nature climate change

LETTERS

https://doi.org/10.1038/s41558-020-0897-7

Check for updates

Weakening Atlantic overturning circulation causes South Atlantic salinity pile-up

Chenyu Zhu[1,2,3] and Zhengyu Liu[4,5] ✉

The Atlantic Meridional Overturning Circulation (AMOC) is an active component of the Earth's climate system[1] and its response to global warming is of critical importance to society. Climate models have shown an AMOC slowdown under anthropogenic warming since the industrial revolution[2–4], but this slowdown has been difficult to detect in the short observational record[5–10] because of substantial interdecadal climate variability. This has led to the indirect detection of the slowdown from longer-term fingerprints[11–14] such as the subpolar North Atlantic 'warming hole'[11]. However, these fingerprints, which exhibit some uncertainties[15], are all local indicators of AMOC slowdown around the subpolar North Atlantic. Here we show observational and modelling evidence of a remote indicator of AMOC slowdown outside the North Atlantic. Under global warming, the weakening AMOC reduces the salinity divergence and then leads to a 'salinity pile-up' remotely in the South Atlantic. This evidence is consistent with the AMOC slowdown under anthropogenic warming and, furthermore, suggests that this weakening has likely occurred all the way into the South Atlantic.

Significant anthropogenic warming has already occurred for many decades, and some signals have already been detected in the surface[16] and deep Atlantic Ocean[17,18]. Since the adjustment time of the AMOC from the North Atlantic to the South Atlantic is at the decadal timescale[19], the signal of AMOC slowdown will have propagated from the subpolar North Atlantic far into the South Atlantic. Physically, this remote AMOC response away from the North Atlantic deep-convection region is possible because the AMOC slowdown under global warming is forced by a slowly increasing surface heat flux over the subpolar North Atlantic[2], and this type of buoyancy-forced AMOC response has been shown to be able to propagate southward coherently against the distortion by variable wind forcing[20–24]. However, there has so far been no observational evidence of a remote AMOC weakening response outside the North Atlantic. Here, by 'remote' response, we refer to the response downstream of the AMOC lower branch, away from the subpolar North Atlantic where deep water formation occurs. Previous indicators, such as the 'warming hole' (Fig. 1b and Extended Data Fig. 1), are all confined locally around the subpolar North Atlantic region[11–14,16]. The deep-warming signal detected recently extending from the North[17] into the South[18] Atlantic is not an indicator of remote AMOC slowdown, because this warming can be generated simply by the advection of a warm anomaly from the North Atlantic in the mean abyssal current. The remote AMOC response, if any, will also be difficult to detect in the SST field outside the subpolar North Atlantic, because, under anthropogenic warming, the bipolar-seesaw SST fingerprint of the AMOC[25,26] could be overwhelmed by the associated surface heating.

Here, we show that the remote response of the AMOC slowdown can be detected in the South Atlantic in a salinity indicator called the Atlantic 'salinity pile-up'. This salinity indicator differs from the traditional 'salty-getting-saltier' fingerprint in the global sea surface salinity (SSS, climatology in Extended Data Fig. 2) identified in observations (Fig. 1a) and models (Fig. 1c,e and Extended Data Figs. 3 and 4)[27–31], which is forced locally by the surface evaporation minus precipitation (E−P)[29] (Fig. 1d,f) through the 'rich-getting-richer' precipitation response (meaning increased (decreased) precipitation in climatologically wetter (drier) regions[32]) and, therefore, is a fingerprint of the intensified atmospheric hydrological cycle only and is irrelevant to the AMOC response. Instead, the Atlantic salinity pile-up refers to a relatively greater trend in basin-mean salinity increase in the subtropical Atlantic than the Indo-Pacific from the surface to the thermocline (>300 to 500 m) (Fig. 2). This salinity pile-up is detectable in the observations (Fig. 1a and last panel of Extended Data Fig. 3) and model ensemble means for both the historical period (Fig. 1c and Extended Data Fig. 3) and future warming scenarios (Fig. 1e and Extended Data Fig. 4). Note that, in the observations or a single model simulation, the detailed SSS-trend pattern within each basin could differ substantially due to other factors such as the local wind-driven gyre and internal climate variability. Our focus here, however, is the basin-mean salinity response, which will be shown to be affected more by the AMOC in response to anthropogenic warming downstream in the South Atlantic. Most interesting here is the comparison between the South Atlantic and South Indo-Pacific in terms of their relationship of basin-mean trends between SSS and the local E−P forcing. For example, in the future warming scenario (Fig. 1e,f), the larger trend in basin-mean salinity increase in the subtropical South Atlantic is accompanied by a smaller trend in E−P increase relative to the Indo-Pacific. Therefore, this salinity pile-up in the South Atlantic relative to the Indo-Pacific cannot be caused simply by local E−P. Given the robust AMOC slowdown across models and the potential reduction of the salinity transport by the AMOC slowdown in the South Atlantic that is absent in the Indo-Pacific, we hypothesize that this salinity pile-up in the South Atlantic is remotely caused by, and therefore is a remote indicator of, the AMOC slowdown. In comparison, the stronger trend in basin-mean salinity increase in the subtropical North Atlantic corresponds to a stronger E−P trend than that over North Pacific and, therefore, could be forced predominantly by the atmosphere[29].

The mechanism of the salinity pile-up can be examined in climate models by statistical analysis and sensitivity experiments. Denoting S'_N as the basin-mean SSS anomaly (from long-term climatological means) for the subtropical North Atlantic (10° N to 40° N) and $\Delta S'_S$ as the difference between the basin-mean SSS anomalies between

[1]Key Laboratory of Physical Oceanography, Ocean University of China, Qingdao, China. [2]Open Studio for Ocean-Climate-Isotope Modeling, Pilot National Laboratory for Marine Science and Technology (Qingdao), Qingdao, China. [3]Department of Atmospheric and Oceanic Sciences, School of Physics, Peking University, Beijing, China. [4]College of Geography Science, Nanjing Normal University, Nanjing, China. [5]Atmospheric Science Program, Department of Geography, Ohio State University, Columbus, OH, USA. ✉e-mail: liu.7022@osu.edu

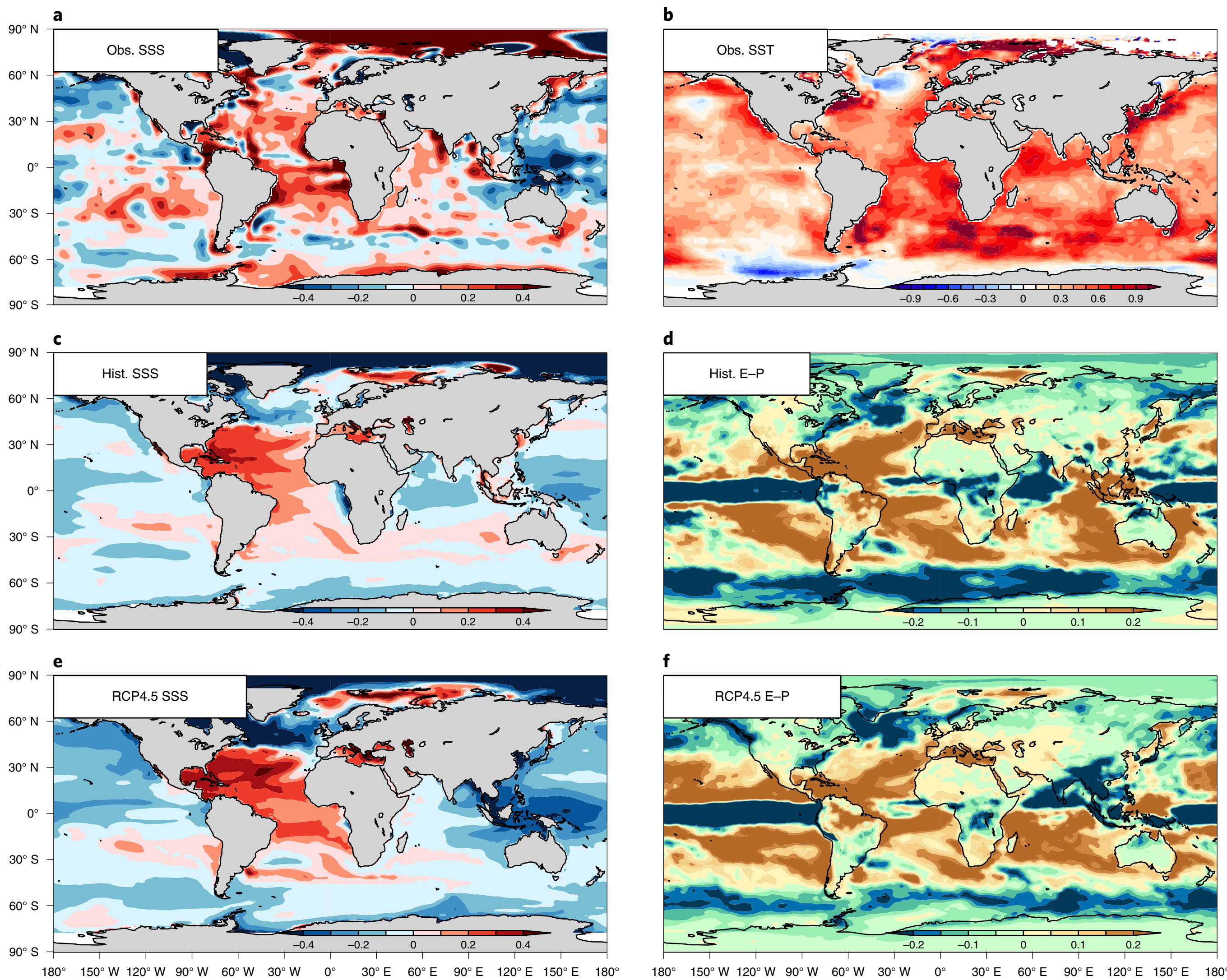

Fig. 1 | Global SSS and SST trends. a–f, Linear trends in SSS (psu century^{-1}) for 1950–2017 (EN4) (**a**); SST (K century^{-1}) (**b**) for 1870–2017 (HadISST) in the observations (Obs.); SSS (**c**) and E−P (mm day^{-1} century^{-1}) (**d**) for ensemble mean historical (Hist.) runs of 1950–2017 (the runs were extended from 2006 to 2017 with simulations of the RCP4.5 scenario) and SSS (**e**) and E−P (**f**) for ensemble mean RCP4.5 runs for 2018–2100. The salinity pile-up in the Atlantic (relative to other oceans) can be seen in the observations, historical run and RCP4.5 run. The weaker E−P trend in the South Atlantic than Indo-Pacific is clear in the RCP4.5 runs; this difference in E−P trends, however, is not very clear in the historical run because of the weaker trend signal, and is difficult to assess in the observations because of the uncertainty in the long-term E−P observations.

the subtropical South Atlantic and Indo-Pacific (10° S to 34° S), we define the salinity indices for the South and North Atlantic salinity pile-ups as $S_S = -\Delta S'_S$ and $S_N = -S'_N$, where the negative sign is chosen to be consistent with the AMOC intensity. (All conclusions drawn below concerning S_S are insensitive to the details of domain choice). The close relationship between the salinity indices and AMOC can be seen first in their annual evolution from 1850 to 2100 in IPCC model simulations (Methods and Fig. 3a). Ensemble-averaged across models, both salinity indices follow the weakening AMOC closely, similarly to the warming hole index T_{NA}, which is defined as the SST anomaly of the subpolar North Atlantic relative to the global mean (Methods)[12]. This seemingly good correlation itself, however, does not provide strong evidence for the salinity indicator, because the ensemble mean filters out internal variability such that the final ensemble-mean signal is dominated by a global warming trend in the last 100 years.

The remote salinity indicator is instead supported by two more stringent statistical measures, again similarly to T_{NA}[11,12]: first, the interannual correlation and, second, the cross-simulation trend correlation, both with AMOC. First, in historical simulations, annual S_S (Fig. 3b) and S_N (Extended Data Fig. 5a) are significantly correlated ($P < 0.1$) with AMOC for most models, with the correlation coefficients somewhat weaker than, but still comparable with, those of T_{NA}. Furthermore, for S_S variability, the AMOC forcing seems to be more dominant than the local E−P forcing, as implied by the stronger correlations of S_S with AMOC compared with those of S_S with E−P in most models (Extended Data Fig. 5b). Given that the historical simulation includes significant internal variability, notably the Atlantic multidecadal variability[33], in addition to a weak trend in its response to anthropogenic warming, we further calculated the correlation by decomposing the time series into internal variability (detrended residual) and trend. The calculation shows that the correlation between S_S and AMOC in the historical run is contributed largely by the internal variability and is enhanced by the weak trend in most models (not shown). Since the contribution of internal variability may be underestimated in models[34], the

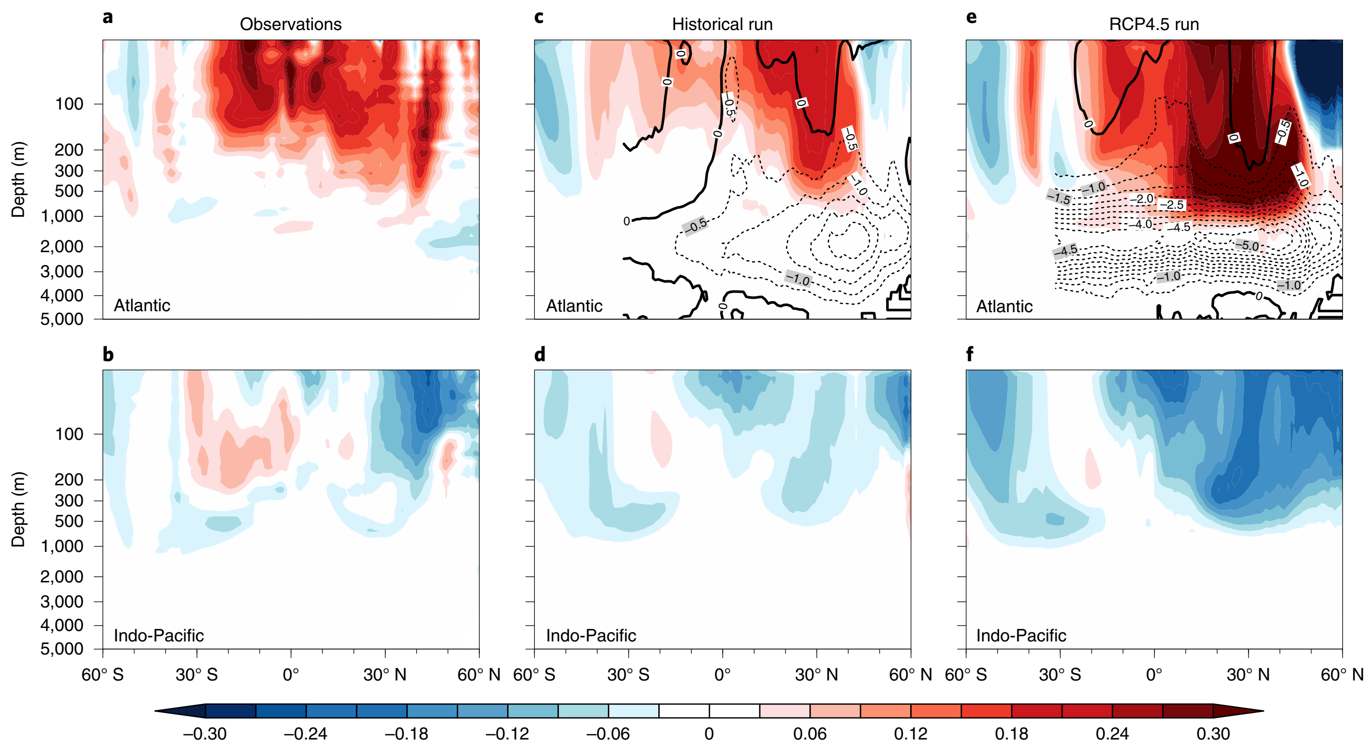

Fig. 2 | Zonal mean salinity trends. a–f, Linear trends in salinity (psu century^{-1}, colour bar) for the Atlantic (**a**) and Indo-Pacific (**b**) in the observations (EN4) (1950–2017); the Atlantic (**c**) and Indo-Pacific (**d**) in the historical run ensemble mean (1950–2017) and the Atlantic (**e**) and Indo-Pacific (**f**) for the RCP4.5 ensemble mean (2018–2100). **c**,**e**, Trends in the AMOC (Sv century^{-1}, contours (represented by solid positive and dashed negative lines); 1 Sv = 10^6 m^3 s^{-1}). The Atlantic salinity pile-up relative to the Indo-Pacific can be seen in all the cases.

contribution of internal variability may be even stronger in the real world. The significant correlation observed for internal variability is further confirmed by calculating the interannual correlation for ten models on their long control simulations that are forced under fixed climate forcing. In all ten control simulations, the correlations between S_S and AMOC are positive, with seven being significant at $P<0.1$. (These correlations are smaller than those between T_{NA} and AMOC, as in the historical runs). In addition, for both S_S and T_{NA}, their correlations with AMOC tend to be maximized when the AMOC leads, suggesting an impact of AMOC on both indicators. The lead of maximum correlation in the different models is less than 5 years for T_{NA}, but ranges from years to decades for S_S. This is reasonable, because the AMOC impacts the warming hole immediately after the local convection adjustment in the subpolar North Atlantic but will affect South Atlantic salinity remotely on a long timescale that may vary widely among models due to different model circulation and internal variability.

Second, the support for the salinity indicator is even stronger in the global warming responses in the trends of S_S (Fig. 3c) and S_N (Extended Data Fig. 6a) across models. These salinity trends are well correlated with the AMOC weakening across warming scenarios ($R=0.76$ for S_S and 0.64 for S_N), as for T_{NA} ($R=0.75$, Extended Data Fig. 6b). This implies that a stronger AMOC slowdown corresponds to a stronger salinity pile-up, especially in the South Atlantic, with a slope of 2.3 Sv/0.1 psu, further supporting the salinity indices. Moreover, for S_S, the trends are highly correlated with the AMOC but have little correlation with the local E−P forcing (Extended Data Fig. 6). The dominant effect of AMOC forcing over local E−P forcing on trends is much stronger than the effect on interannual correlations (Extended Data Fig. 5b), implying a more dominant role of the AMOC on longer timescales. This is consistent with the coherent dynamic response of the AMOC to buoyancy forcing occurring preferentially over longer timescales[20–24]. In comparison, for S_N, the E−P forcing becomes important (almost as important as the AMOC) as seen in both the interannual correlation (Extended Data Fig. 5c versus 5b) and trend correlation (Extended Data Fig. 6d versus 6c). The two correlation analyses above suggest that the South Atlantic salinity pile-up can serve as a new indicator for AMOC changes, from internal climate variability to long-term trends.

Our salinity indicators imply, consistently with T_{NA}, that a remote weakening response of the AMOC is possible in the observations in the span of 1900–2017 (Fig. 3d). In spite of strong decadal variability, both S_S and S_N show a weakening trend after the 1960s, similar to that of T_{NA}. For the last one to two decades, the inferred AMOC weakening trends in all three indices also appear to be consistent in sign with the observed AMOC trends in the direct RAPID measurements[6–8], a reanalysis (GloSea5)[35] over the North Atlantic and the reconstruction with Argo and altimetry in the South Atlantic[9] (Fig. 3b). There are, nevertheless, some differences: T_{NA} exhibits a strong interdecadal variability starting from the 1950s, while S_N and S_S decrease smoothly starting from the 1970s. The differences among indicators could be caused by the distortion of natural interdecadal variability, especially that associated with wind variability[20–24]; by the signal of the AMOC decline being weak, as inferred from the large ensemble spreads; or, finally, by uncertainties in the three indices in the historical simulations (Fig. 3a and Extended Data Figs. 5 and 6). Indeed, natural variability is also likely responsible for different timings of initial AMOC decline estimated in the observations, even among various North Atlantic local temperature indicators[11–13]. Relative to S_S, T_{NA} may also be affected more directly by radiative forcing and shorter Atlantic decadal variability, especially in the last half-century when both the variability and discrepancy are large.

We further show that the South Atlantic salinity pile-up is caused remotely by AMOC slowdown, as already inferred from

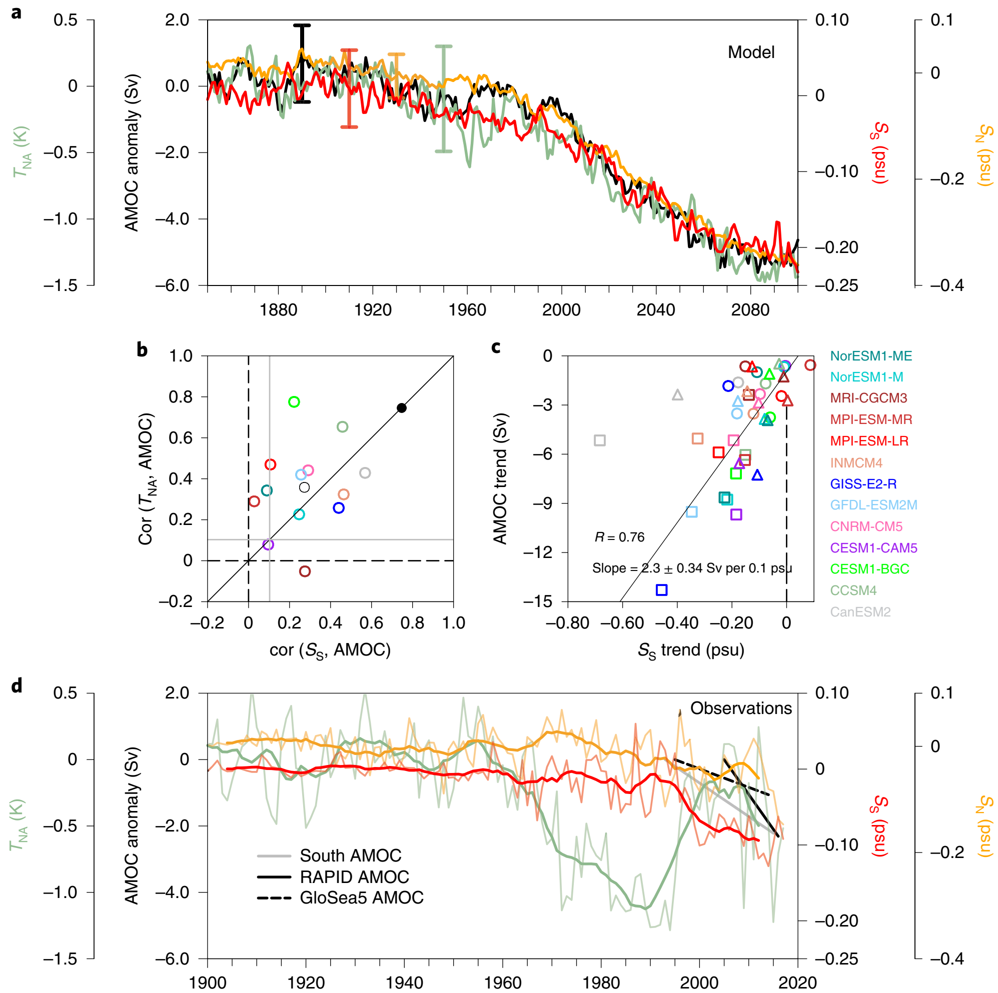

Fig. 3 | Evolution of AMOC and its indicators. a, Time series of the ensemble mean annual AMOC transport (black), S_N (orange), S_S (red) and T_{NA} (green) in the combined historical-to-future RCP4.5 scenario simulations (1850–2100), with the error bars on the left side denoting cross-simulation spread (±1 s.d.) averaged over the historical period. **b**, Scatter plot of the instantaneous interannual correlation coefficients of annual AMOC and T_{NA} versus AMOC and S_S for the historical period of 1861–2018 (2006–2018 extended with the RCP8.5 scenario simulations) across models. The black solid line represents the 1:1 diagonal line, grey lines represent $P = 0.1$ significance, dashed lines represent the zeros and the filled black circle represents the model ensemble mean. **c**, Scatter plot of the trends of AMOC versus S_S for historical (1861–2018, circles), RCP4.5 (2019–2100, triangles) and RCP8.5 (2019–2100, squares) simulations for each model. The solid line represents the regression line and the dashed line represents the zero S_S trend (additional information related to **b** and **c** is shown in Extended Data Figs. 5 and 6). Correlation and linear regression analyses were performed with $n = 36$ simulations, with model CanESM2 (grey) excluded as an outlier. $R = 0.76$, $P < 0.01$. **d**, Time series of S_N (orange), S_S (red, EN4) and T_{NA} (green, HadISST) in the observations. Thin lines are the annual means, while the thick lines are the 10-year running means. Also shown are the trends of annual mean AMOC transport across 26.5° N in the North Atlantic monitored in the RAPID project (2005–2016, solid black line) and an ocean reanalysis product GloSea5 (1995–2014, dashed black line) as well as a reconstruction from Argo and altimetry averaged across 20° S, 25° S and 30° S in the South Atlantic (1993–2015, grey line). All the time series are anomalies relative to the means of 1900–1950, except the three short AMOC measurements, for which the trend line starts from the first year of each.

the much stronger impact of the AMOC on S_S than E−P in both interannual and cross-simulation correlations (Extended Data Figs. 5b and 6c). We first show that this salinity pile-up is caused by circulation changes in the salinity budget in a coupled simulation (Methods). With global warming, E−P increases less in the South Atlantic than in the Indo-Pacific, while salinity increases more in the South Atlantic (as discussed in Fig. 1e,f). The salinity pile-up is caused by a smaller increase in salinity divergence in the South Atlantic than in the Indo-Pacific relative to their respective increases in E−P forcing (Extended Data Fig. 7). The changes in salinity divergence are mainly driven by the effect of the circulation change on mean salinity (not shown). This circulation change is induced substantially by the weakening AMOC.

The impact of the AMOC on S_S is shown more clearly in ocean-alone sensitivity experiments, which are forced by anomalous surface buoyancy forcing and are therefore not influenced by wind forcing (Methods). The global warming impact of E−P forcing is simulated in experiment EmP, which is forced by the E−P trend of the ensemble mean RCP4.5 experiment (Fig. 1f), while the impact of a weakening AMOC is simulated in experiment HFX, which is forced by a spatially uniform surface heat flux trend. As expected, E−P forcing alone (EmP) produces a pattern of upper-ocean salinity similar to E−P, and salinity piles up (relative to the Indo-Pacific) in the North Atlantic but not in the South Atlantic (Fig. 4c and Extended Data Fig. 8c,d); the dominant effect of E−P forcing on South Atlantic salinity can also be seen in the salinity budget

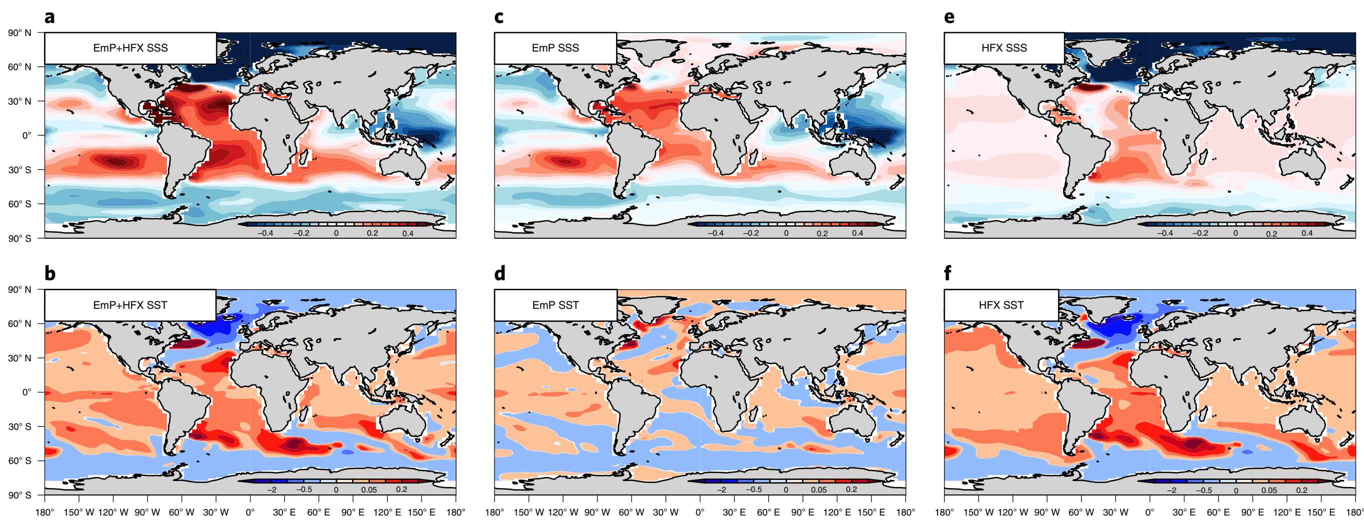

Fig. 4 | SSS and SST trends in ocean sensitivity experiments. a–f, Trends in SSS (psu century^{-1}) (**a**,**c**,**e**) and SST (K century^{-1}) (**b**,**d**,**f**) in ocean model experiments forced by a trend in the combined E−P flux and heat flux (EmP+HFX) (**a**,**b**), the E−P flux only (EmP) (**c**,**d**) and a globally uniform heat flux (HFX) (**e**,**f**). The experiments show that the weakening of the AMOC under heat flux forcing generates a salinity pile-up in the South Atlantic as well as a warming hole in the subpolar North Atlantic.

(Extended Data Fig. 9c). Note that there is no warming hole (Fig. 4d), because the AMOC remains little changed (Extended Data Fig. 8c). In contrast, under the heat flux forcing (HFX), the AMOC weakens substantially[2] (Extended Data Fig. 8e) and then generates a distinct salinity pile-up remotely in the South Atlantic (relative to the Indo-Pacific) (Fig. 4e and Extended Data Fig. 8e,f), as well as the warming hole in the subpolar North Atlantic (Fig. 4f). Consistent with buoyancy-forced responses in previous studies[21–24], the AMOC response expands southward coherently into the South Atlantic, inducing warming and salinity pile-up in the upper South Atlantic (Extended Data Fig. 9e–g). Under HFX, salinity divergence is reduced (Extended Data Fig. 9d) by the decreased AMOC export in the South Atlantic, which, in a further decomposition, is caused by the weakening AMOC circulation. Combined, E−P and heat flux force the salinity pile-up in both the South and North Atlantic, as well as the warming hole in experiment EmP+HFX (Fig. 4a,b and Extended Data Fig. 8a,b), consistent with the coupled experiment (Figs. 1e and 2e,f). In comparison with experiment EmP, the salinity budget further confirms that the weakening AMOC reduces salinity divergence and, in turn, piles up salinity over the South Atlantic (Extended Data Fig. 9b,c), mainly due to the change in circulation. The mechanism of the South Atlantic salinity pile-up is summarized schematically in Extended Data Fig. 10, along with the budget of upper Atlantic salinity transport in experiment HFX. With the reduction of the AMOC, the northward salinity transport in the upper South Atlantic is reduced relative to the control climatology (Extended Data Fig. 10a). In the upper branch of the AMOC, the reduction in salinity transport is greater downstream (on the northern side) than upstream (southern side) because of a greater mean salinity on the northern side, leading first to anomalous salinity convergence and then to salinity pile-up in the South Atlantic (Extended Data Fig. 10b).

In short, we have provided evidence of a remote signal of AMOC slowdown under anthropogenic warming in the South Atlantic, far removed from the subpolar North Atlantic, in models and, likely, observations. This remote echo of the AMOC is projected to intensify with global warming and further AMOC slowdown.

Online content

Any methods, additional references, Nature Research reporting summaries, source data, extended data, supplementary information, acknowledgements, peer review information; details of author contributions and competing interests; and statements of data and code availability are available at https://doi.org/10.1038/s41558-020-0897-7.

Received: 22 March 2019; Accepted: 4 August 2020;
Published online: 14 September 2020

References

1. Buckley, M. W. & Marshall, J. Observations, inferences, and mechanisms of Atlantic Meridional Overturning Circulation variability: a review. *Rev. Geophys.* **54**, 5–63 (2016).
2. Gregory, J. M. et al. A model intercomparison of changes in the Atlantic thermohaline circulation in response to increasing atmospheric CO_2 concentration. *Geophys. Res. Lett.* **32**, l12703 (2005).
3. IPCC *Climate Change 2013: The Physical Science Basis* (eds Stocker, T. F. et al.) (Cambridge Univ. Press, 2013).
4. Liu, W. et al. Overlooked possibility of a collapsed Atlantic Meridional Overturning Circulation in warming climate. *Sci. Adv.* **3**, e1601666 (2017).
5. Bryden, H. L., Longworth, H. R. & Cunningham, S. A. Slowing of the Atlantic Meridional Overturning Circulation at 25° N. *Nature* **438**, 655–657 (2005).
6. Robson, J., Hodson, D., Hawkins, E. & Sutton, R. Atlantic overturning in decline? *Nat. Geosci.* **7**, 2–3 (2014).
7. Smeed, D. A. et al. Observed decline of the Atlantic Meridional Overturning Circulation 2004–2012. *Ocean Sci.* **10**, 29–38 (2014).
8. Srokosz, M. A. & Bryden, H. L. Observing the Atlantic Meridional Overturning Circulation yields a decade of inevitable surprises. *Science* **348**, 1255575 (2015).
9. Majumder, S., Schmid, C. & Halliwell, G. An observations and model based analysis of meridional transports in the South Atlantic. *J. Geophys. Res. Oceans* **121**, 5622–5638 (2016).
10. Smeed, D. A. et al. The North Atlantic Ocean is in a state of reduced overturning. *Geophys. Res. Lett.* **45**, 1527–1533 (2018).
11. Rahmstorf, S. et al. Correction: Corrigendum: Evidence for an exceptional twentieth-century slowdown in Atlantic Ocean overturning. *Nat. Clim. Change* **5**, 956 (2015).
12. Caesar, L. et al. Observed fingerprint of a weakening Atlantic Ocean overturning circulation. *Nature* **556**, 191–196 (2018).
13. Thornalley et al. Anomalously weak Labrador Sea convection and Atlantic overturning circulation during the past 150 years. *Nature* **556**, 227–230 (2018).
14. Thibodeau, B. et al. Last century warming over Canadian Atlantic shelves linked to weaker Atlantic Meridional Overturning Circulation. *Geophys. Res. Lett.* https://doi.org/10.1029/2018GL080083 (2018).

15. Moffa-Sanchez, P. et al. Variability in the northern North Atlantic and Arctic oceans across the last two millennia: a review. *Paleoceanogr. Paleoclimatol.* https://doi.org/10.1029/2018PA003508 (2019).
16. Chemke, R., Zanna, L. & Polvani, L. M. Identifying a human signal in the North Atlantic warming hole. *Nat. Commun.* **11**, 1540 (2020).
17. Chen, X. & Tung, K. K. Global surface warming enhanced by weak Atlantic overturning circulation. *Nature* **559**, 387–391 (2018).
18. Zhang, M., Wu, Z. & Qiao, F. Deep Atlantic Ocean warming facilitated by the deep western boundary current and equatorial Kelvin waves. *J. Clim.* **31**, 8541–8555 (2018).
19. Johnson, H. & Marshall, D. A theory for the surface Atlantic response to thermohaline variability. *J. Phys. Oceanogr.* **32**, 1121–1132 (2002).
20. Bingham, R. J., Hughes, C. W., Roussenov, V. & Williams, R. G. Meridional coherence of the North Atlantic Meridional Overturning Circulation. *Geophys. Res. Lett.* **34**, 4–9 (2007).
21. Biastoch, A., Böning, C. W., Getzlaff, J., Molines, J. M. & Madec, G. Causes of interannual–decadal variability in the meridional overturning circulation of the midlatitude North Atlantic ocean. *J. Clim.* **21**, 6599–6615 (2008).
22. Zhang, R. Coherent surface–subsurface fingerprint of the Atlantic Meridional Overturning Circulation. *Geophys. Res. Lett.* **35**, L20705 (2008).
23. Lozier, M. S. Overturning in the North Atlantic. *Annu. Rev. Mar. Sci.* **4**, 291–315 (2012).
24. Gu, S., Liu, Z. & Wu, L. Timescale dependence of the meridional coherence of Atlantic Meridional Overturning Circulation. *J. Geophys. Res. Oceans* https://doi.org/10.1029/2019JC015838 (2020).
25. Stocker, T. F. & Johnsen, S. J. A minimum thermodynamic model for the bipolar seesaw. *Paleoceanography* **18**, 1087 (2003).
26. Shakun, J. et al. Global warming preceded by increasing CO_2 during the last deglaciation. *Nature* **484**, 49–54 (2012).
27. Boyer, T. P. et al. Linear trends in salinity for the world ocean, 1955–1998. *Geophys. Res. Lett.* **32**, L01604 (2005).
28. Hosoda, S., Sugo, T., Shikama, N. & Mizuno, K. Global surface layer salinity change detected by Argo and its implication for hydrological cycle intensification. *J. Oceanogr.* **65**, 579–586 (2009).
29. Durack, P. J., Wijffels, S. E. & Matear, R. J. Ocean salinities reveal strong global water cycle intensification during 1950–2000. *Science* **336**, 455–458 (2012).
30. Skliris, N. et al. Salinity changes in the world ocean since 1950 in relation to changing surface freshwater fluxes. *Clim. Dyn.* **43**, 709–736 (2014).
31. Lago, V. et al. Simulating the role of surface forcing on observed multidecadal upper-ocean salinity changes. *J. Clim.* **29**, 5575–5588 (2016).
32. Held, I. M. & Soden, B. J. Robust responses of the hydrological cycle to global warming. *J. Clim.* **19**, 5686–5699 (2006).
33. Zhang, R. et al. A review of the role of the Atlantic Meridional Overturning Circulation in Atlantic multidecadal variability and associated climate impacts. *Rev. Geophys.* **57**, 316–375 (2019).
34. Yan, X., Zhang, R. & Knutson, T. R. Underestimated AMOC variability and implications for AMV and predictability in CMIP models. *Geophys. Res. Lett.* **45**, 4319–4328 (2018).
35. Jackson, L. C., Peterson, K. A., Roberts, C. D. & Wood, R. A. Recent slowing of Atlantic overturning circulation as a recovery from earlier strengthening. *Nat. Geosci.* **9**, 518–522 (2016).

Publisher's note Springer Nature remains neutral with regard to jurisdictional claims in published maps and institutional affiliations.

Methods

CMIP5 model simulations. We use the model output of a total of 13 CMIP5 models: CanESM2, CCSM4, CESM1-BGC, CESM1-CAM5, CNRM-CM5, GFDL-ESM2M, GISS-E2-R, INMCM4, MPI-ESM-LR, MPI-ESM-MR, MRI-CGCM3, NorESM1-M and NorESM1-ME. We analyse the time period 1850–2100, covering the historical run and two future scenarios (RCP4.5 and RCP8.5) as well as control runs with various model integration lengths. The ensemble mean is calculated with equal weight on each simulation. Model data are interpolated to the observation grid points before calculation. All these simulations are publicly available at http://www.ipcc-data.org/sim/gcm_monthly/AR5/Reference-Archive.html.

Datasets. We use two observational datasets for salinity. The first is the ISHII data[36] version 6.13 (https://rda.ucar.edu/datasets/ds285.3/), which includes the objectively analysed subsurface temperature and salinity of 24 levels in the upper 1,500 m, with1° × 1° resolution, during 1945–2012. The second is the monthly mean ocean salinity from Hadley Centre EN4 dataset version 4.2.1 (ref. [37]) (https://www.metoffice.gov.uk/hadobs/en4/download-en4-2-1.html) with the Levitus correction[38]. This is a quality-controlled ocean dataset of in situ observations objectively mapped onto a global 1° × 1° grid for 1900–2017. The observational SST is HadISST[39] from the Hadley Centre, which is a unique combination of monthly globally complete fields of SST and sea ice concentration on a 1° × 1° grid from 1870 to 2017 (https://www.metoffice.gov.uk/hadobs/hadisst/).The direct measurements of the AMOC in the RAPID array along 26.5° N are publicly available on www.rapid.ac.uk/rapidmoc/rapid_data/. The GloSea5 reanalysis data were provided by L. Jackson[35]. The South Atlantic AMOC data derived from Argo and altimetry are freely available from www.aoml.noaa.gov/phod/samoc_argo_altimetry/index.php. The Community Earth System Model (CESM) Large Ensemble (CESM-LE) data[40] can be found at http://www.cesm.ucar.edu/projects/community-projects/LENS/. The POP2 data of sensitivity experiments used in this study are available from the corresponding author upon request.

Definition of AMOC strength and the SST-based AMOC index. AMOC intensity is defined as the maximum overturning stream function below 300 m over 30° N to 50° N in the Atlantic. The SST-based AMOC index T_{NA} is calculated following its latest version as proposed in Caesar et al.[12], except that the annual mean data are used instead of the November–May season data. First, we calculate the SST trend on each grid point over the globe for the period 1850–2100 with the global mean SST trend subtracted. This tends to generate a cooling in the subpolar North Atlantic and warming along the Gulf Stream region (Extended Data Fig. 1). We then use the area-weighted SST averaged over the cooling region in the subpolar North Atlantic as the SST-based AMOC index T_{NA} for each ensemble member. The ensemble mean T_{NA} is then calculated with each member equally weighted.

Salinity budget and analysis. The salinity budget for the upper 300 m is calculated offline using the monthly output based on the tracer transport equation,

$$\int_0^H \frac{\partial S}{\partial t} = (E - P) \times S_0 - \int_0^H \nabla\left(\vec{v} \times S\right) + \int_0^H \text{mix}$$

Here S and H represent the salinity and layer depth, respectively, and $S_0 = 34.7$ is a reference salinity. The salinity tendency ($\partial S/\partial t$) is determined by the three right-hand side terms above, which are, from left to right, the surface net freshwater flux, ocean salinity transport divergence and interior mixing. The $\vec{v} \times S$ is the three-dimensional salinity transport by the resolved flow (Eulerian mean velocity). The mixing term (including diffusion and unresolved transport induced by eddy and submesoscale processes) in the offline scheme is diagnosed as a residual term. A comparison of our offline scheme with the online scheme (using the last 10 years' data from a default 900 year POP2 control run with online advection and mixing output) over specified regions shows that the offline calculation of salinity advection (or transport divergence) and the residual term using monthly freshwater flux, velocity and salinity output accurately reproduce the online calculation of advection and mixing terms, respectively (not shown).

The salinity budget is applied to one member of the CESM-LE in the RCP8.5 scenario. For the mean climatology, the salinity tendency is determined by a positive source from net E−P and a negative sink of divergence in salinity transport (Extended Data Fig. 7a). With global warming, the accumulated E−P increases (becomes more positive) in both the South Atlantic and Indo-Pacific, overwhelming the increased salinity transport divergence (which becomes more negative) and therefore increasing the salinity in both regions (Extended Data Fig. 7b). The accumulated E−P increases much more in the South Indo-Pacific than in the South Atlantic (Extended Data Fig. 7b), consistent with the discussion of Fig. 1e,f above. This large E−P increase in the Indo-Pacific, however, is largely balanced by a greater salinity divergence and therefore leaves little salinity increase in that region. In contrast, over the South Atlantic, salinity is increased much more than over the Indo-Pacific in spite of a smaller E−P increase, because the salinity divergence is enhanced only slightly, such that a smaller E−P trend in the South Atlantic can still drive a larger SSS increase than in the Indo-Pacific. This smaller increase in salinity divergence in the South Atlantic (relative to the Indo-Pacific) is caused remotely by the weakening AMOC, as demonstrated in ocean-alone experiments below. In comparison, a similar budget analysis shows that in the North Atlantic, the effect of circulation change on salinity divergence is less than the effect of E−P (not shown).

Ocean model and sensitivity experiments. Our ocean model is POP2 (refs. [41,42]), which is the ocean component of the coupled CESM model. Our version of POP2 has a uniform resolution of 3.6° in the zonal direction and a non-uniform resolution in the meridional direction (0.6° near the equator gradually increasing to the maximum of 3.4° at 35° N/S and then decreasing polewards). The model has 60 levels in the vertical. In the upper 160 m, it has a uniform resolution of 10 m. The resolution then decreases towards depth, reaching a resolution of 250 m at a depth of 3,500 m. From 3,500 m towards depth, it has a uniform resolution of 250 m. The control run is forced by the normal year forcing from the Coordinated Ocean–Ice Reference Experiments (CORE) dataset[43], using the CORE experimental design as outlined in Griffies et al.[44]. The CORE forcing and bulk formulae used here are the version 2 (COREv2) as defined in Large and Yeager[43].

Due to a fresh bias, the default POP2 shows an unrealistically shallow late-winter mixed layer (<200 m) around the Labrador Sea and east of Greenland, where the observations show a deepest mixed layer depth of over 1,000 m. Instead, the deepest mixed layer in the model occurs in the Greenland, Iceland and Norwegian Seas. As a remedy, we performed a flux adjustment on salinity. First, a restoring run restarting from a 900 year default control run is performed with an additional surface restoring term added such that SSS is restored towards its observational monthly climatology over the globe with a restoring time of 90 days (upper 50 m). After 300 years of integration, both the AMOC and Labrador Sea mixed layer are found to be near quasi-equilibrium. Then the seasonal cycle of the restoring term is diagnosed from the last 10 years of the restoring run and is added to the model as the surface flux adjustment term. The flux adjustment run is then integrated for another 200 years and exhibits a more realistic mixed layer around the Labrador Sea and Greenland. This flux adjustment run is used as our control run from which the three sensitivity experiments are launched. Sensitivity experiments are integrated for 100 years (corresponding to model years 1401–1500). The wind stress remains unchanged in all experiments so that there is no effect of wind-induced circulation change. As such, the dynamic effect on salinity transport is caused by the buoyancy-forced AMOC change only.

The first experiment (EmP) is designed to study the SSS response to E−P forcing in the global warming scenario. Thus, the anomalous E−P forcing uses the trend of the ensemble mean E−P of the RCP4.5 scenario as demonstrated in Fig. 1f (the results are similar if CESM E−P forcing is used) while the magnitude of the anomalous E−P forcing is increased linearly from zero to its full strength over 100 years, resembling the RCP4.5 scenario integrated from 2006 to 2100. To isolate the salinity response to local E−P forcing in the subtropical ocean and avoid the additional effect of AMOC transport change, the E−P forcing is applied south of 53° N over the globe, avoiding a substantial reduction of the AMOC (Extended Data Fig. 8c) forced by the high latitude freshwater flux. The second experiment (HFX) is designed to identify the responses of both the salinity and temperature to a weakening AMOC in the absence of the E−P trend forcing. Since the increased downward surface heat flux is the major forcing for the weakening AMOC in response to global warming[2], we apply a globally uniform heat flux anomaly over the ocean with the magnitude increasing linearly from 0 to 5 W m^{-2} in 100 years. By this time, the AMOC has been reduced by ~10 Sv (Extended Data Fig. 8e). The third experiment (EmP+HFX) combines both the E−P and heat flux forcing in experiments EmP and HFX. Finally, we note that we have performed extensive sensitivity experiments, which all confirm our major conclusion that the salinity pile-up in the South Atlantic is caused by the weakening AMOC transport. For example, in a set of parallel sensitivity experiments in the default model (without flux adjustment), the results are similar, except that the warming hole is shifted from the Labrador Sea into the Greenland, Iceland and Norwegian Seas in experiments HFX and EmP+HFX.

Data availability

All data used are publicly available online, as described in detail in the Dataset section of Methods. In addition, the POP2 data of the sensitivity experiments used in this study are available from the corresponding author upon request.

Code availability

POP2 is freely available as open-source code from http://www.cesm.ucar.edu/models/cesm1.1.

References

36. Ishii, M., Kimoto, M., Sakamoto, K. & Iwasaki, S. I. Steric sea level changes estimated from historical ocean subsurface temperature and salinity analyses. *J. Oceanogr.* **62**, 155–170 (2006).
37. Good, S. A., Martin, M. J. & Rayner, N. A. EN4: quality controlled ocean temperature and salinity profiles and monthly objective analyses with uncertainty estimates. *J. Geophys. Res. Oceans* **118**, 6704–6716 (2013).

38. Levitus, S. et al. Global ocean heat content 1955–2008 in light of recently revealed instrumentation problems. *Geophys. Res. Lett.* **36**, L07608 (2009).
39. Rayner, N. A. et al. Global analyses of sea surface temperature, sea ice, and night marine air temperature since the late nineteenth century. *J. Geophys. Res.* **108**, 4407 (2003).
40. Kay, J. E. et al. The Community Earth System Model (CESM) large ensemble project: a community resource for studying climate change in the presence of internal climate variability. *Bull. Am. Meteorol. Soc.* **96**, 1333–1349 (2015).
41. Smith, R. D. et al. *The Parallel Ocean Program (POP) Reference Manual: Ocean Component of the Community Climate System Model (CCSM)* Technical Report LAUR-10-01853 (Los Alamos National Laboratory, 2010); http://www.cesm.ucar.edu/models/cesm1.0/pop2/doc/sci/POPRefManual.pdf
42. Danabasoglu, G. et al. The CCSM4 ocean component. *J. Clim.* **25**, 1361–1389 (2012).
43. Large, W. G. & Yeager, S. *Diurnal to Decadal Global Forcing for Ocean and Sea-ice Models: The Data Sets and Flux Climatologies* No. NCAR/TN-460+STR (University Corporation for Atmospheric Research, 2004); https://doi.org/10.5065/D6KK98Q6
44. Griffies, S. M. et al. Coordinated ocean–ice reference experiments (COREs). *Ocean Model.* **26**, 1–46 (2009).

Acknowledgements
We thank C. He, Q. Wen, S. Gu and J. Lynch-Stieglitz for discussions and L. Jackson for providing the GlobSea5 data. We acknowledge the high-performance computing support from NCAR's Computational and Information Systems Laboratory (CISL). This work is supported by the Natural Science Foundation of China Grant 41630527, Ministry of Science and Technology 2017YFA0603801, US National Science Foundation (NSF) projects 1656907 and 1810681 and the Chinese Scholarship Council (CSC).

Author contributions
Z.L. and C.Z. designed the study, C.Z. performed the analysis and experiments and Z.L. wrote the paper with input from C.Z.

Competing interests
The authors declare no competing interests.

Additional information
Extended data Extended data is available for this paper at https://doi.org/10.1038/s41558-020-0897-7.

Correspondence and requests for materials should be addressed to Z.L.

Peer review information *Nature Climate Change* thanks Thomas Haine, Liping Zhang and the other, anonymous, reviewer(s) for their contribution to the peer review of this work.

Reprints and permissions information is available at www.nature.com/reprints.

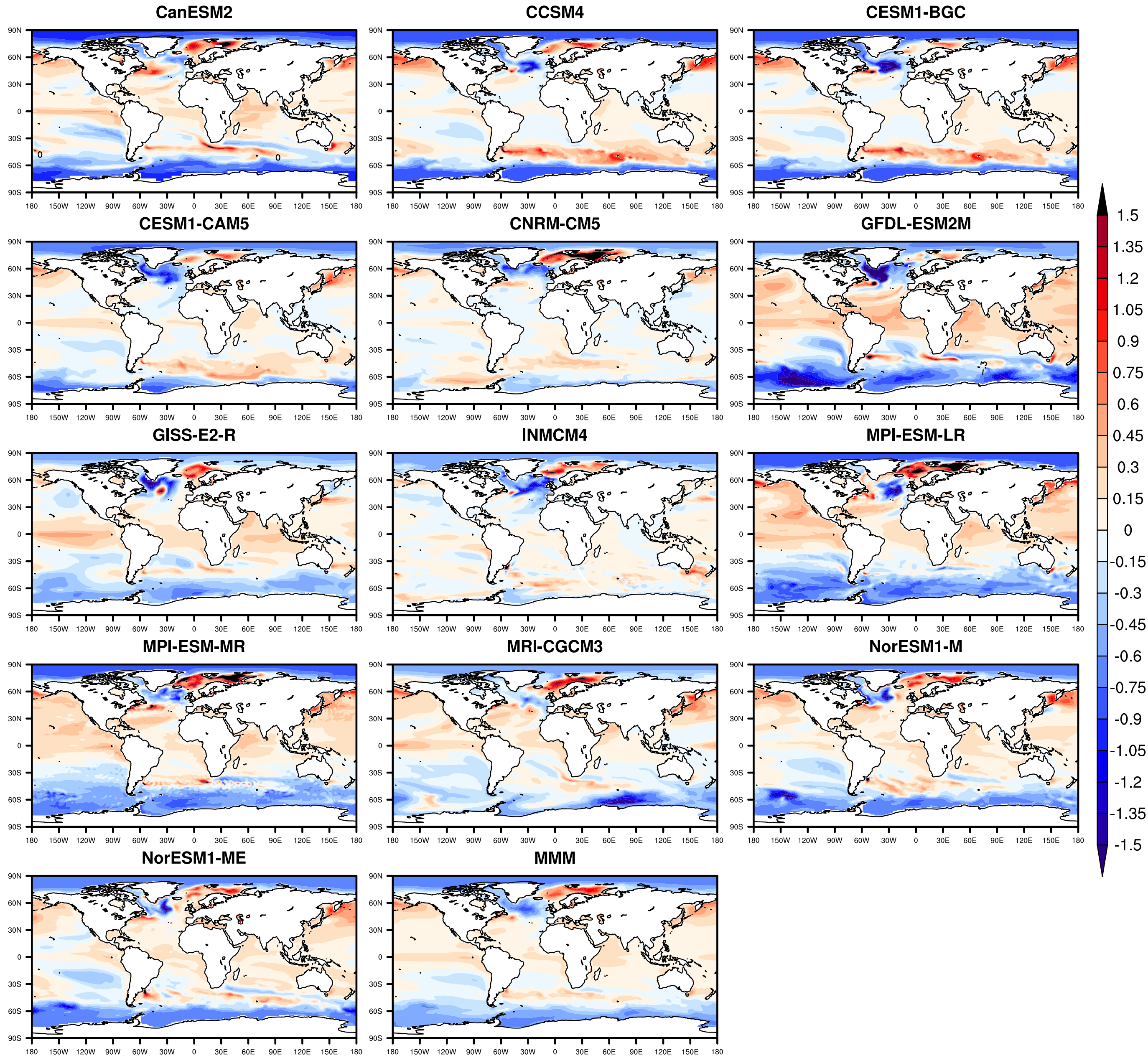

Extended Data Fig. 1 | Model SST trends under global warming. Global pattern of SST trends (relative to the global mean) (K century^{-1}) for 1850–2100 (from 2006 to 2017 with simulations of RCP4.5 scenario) in individual IPCC models and the multi-model mean (MMM).

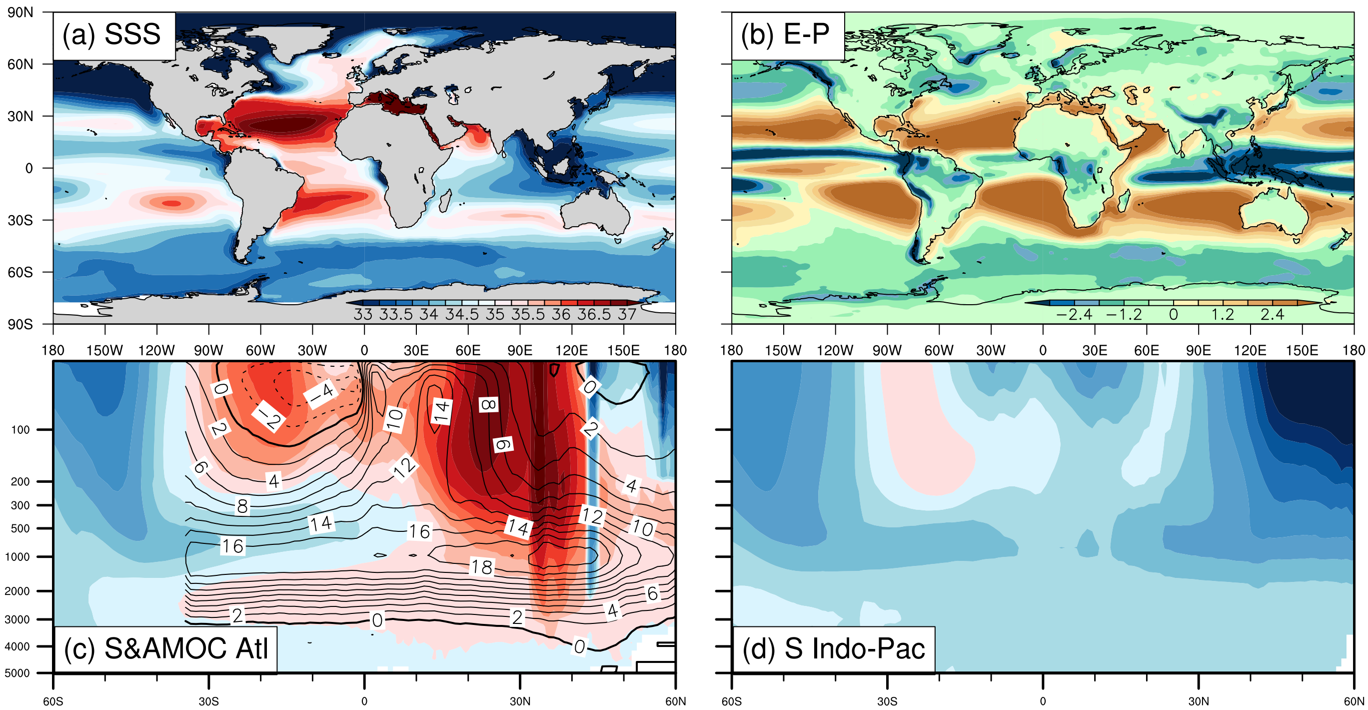

Extended Data Fig. 2 | Model climatology. a–d, Ensemble mean model climatologies (1980–2005). **a**, Annual mean SSS (psu). **b**, E−P (mm day^{-1}). **c**, Atlantic zonal mean salinity (psu, shading) and AMOC stream function (Sv, contours). **d**, Indo-Pacific zonal mean salinity (psu). Panels **c** and **d** share the colour bar of **a**.

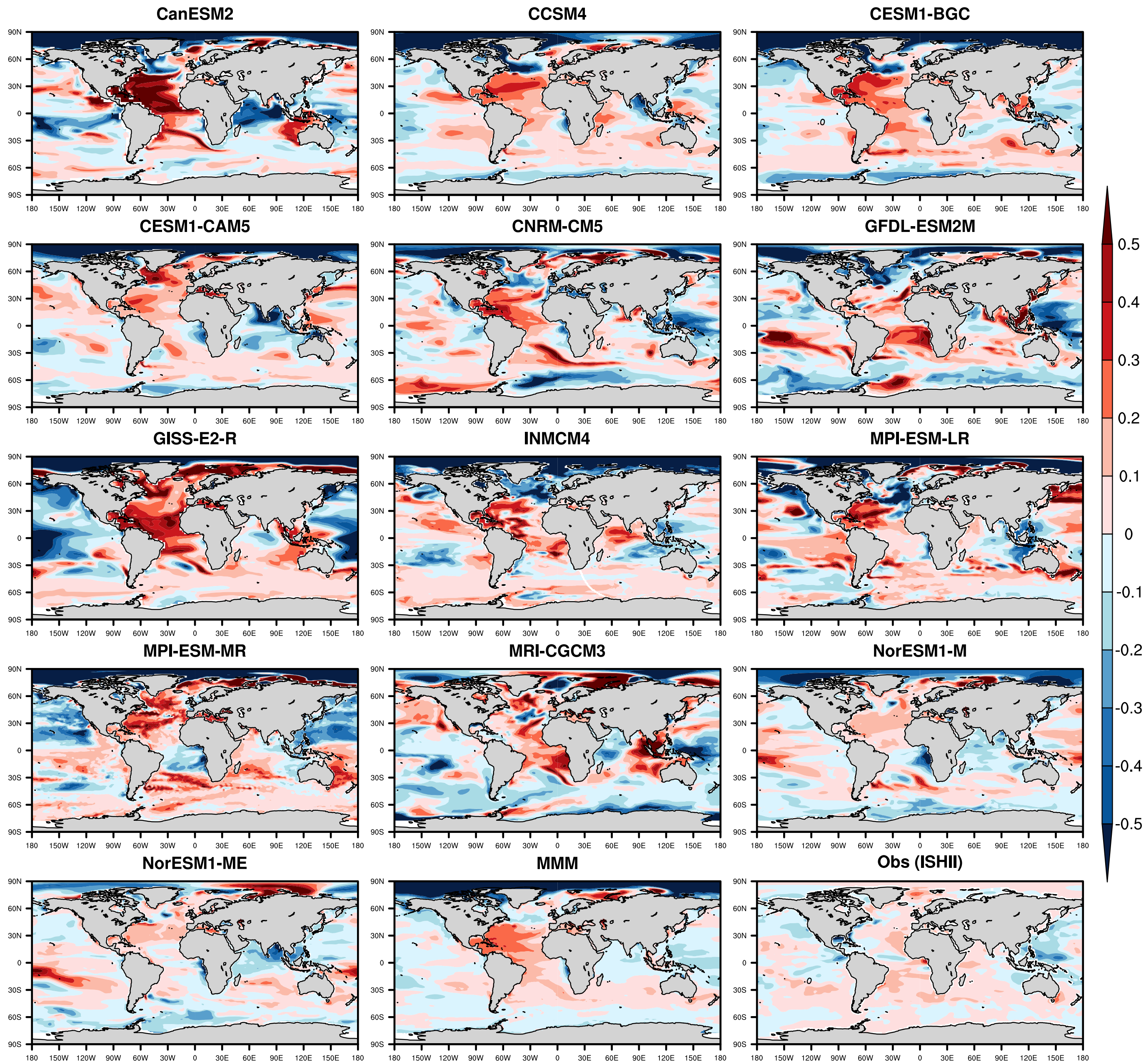

Extended Data Fig. 3 | Model SSS trends in the historical period. Global pattern of SSS trends (relative to the global mean) (psu century^{-1}) for the period of 1945–2012 in individual models and the multi-model mean in the historical runs. The trend in another observational dataset, ISHII, is plotted in the bottom right panel.

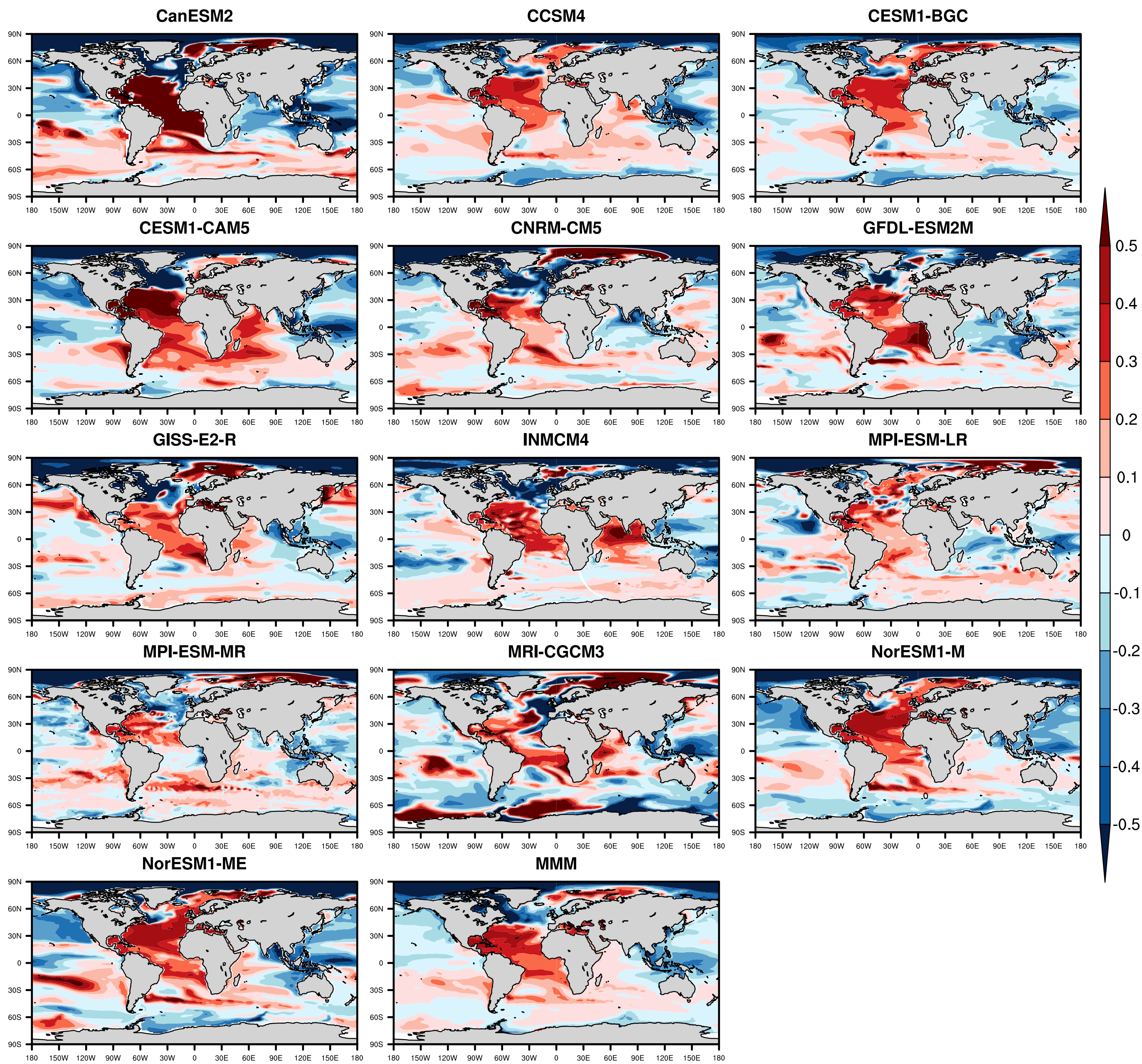

Extended Data Fig. 4 | Model SSS trends under global warming. Global pattern of SSS trends (relative to the global mean) (psu century^{-1}) in individual models and the multi-model mean for the period of 2018–2100 in the RCP4.5 scenario.

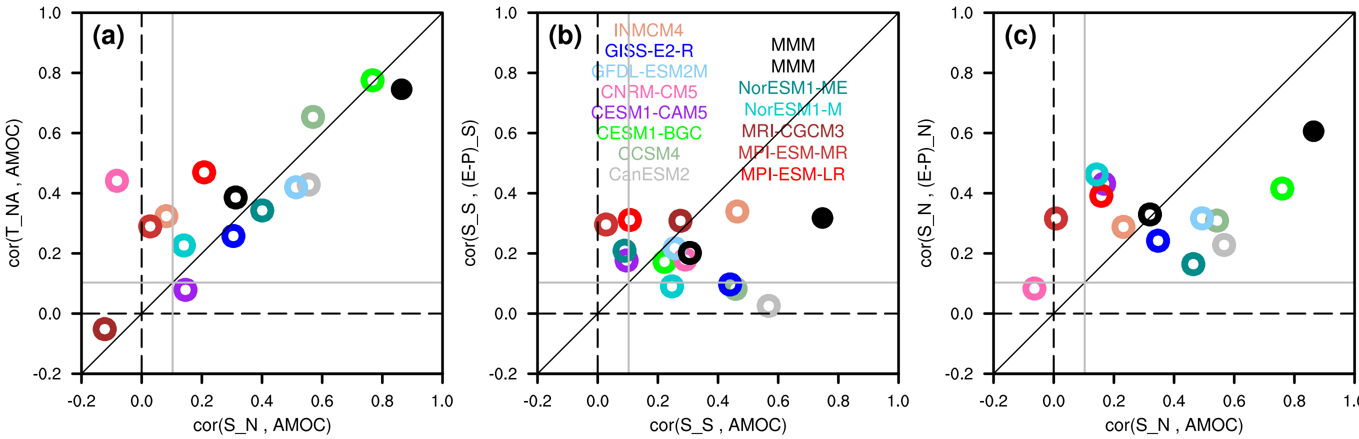

Extended Data Fig. 5 | Temporal correlations among the interannual variability of AMOC, fingerprint indices and E−P. a–c, Cross-model scatter plot of the temporal correlations between the annual mean AMOC and T_{NA} versus those between AMOC and S_N (**a**), (E−P)$_S$ and S_S versus AMOC and S_S (**b**) and (E−P)$_N$ and S_N versus AMOC and S_N (for comparison with 'S' in **b**, here 'N' represents the difference of North Atlantic with North Pacific) for the historical period (1861–2018 with 2006–2018 from the RCP8.5 simulation) (**c**). In each panel, the average of the correlations is shown by open black circles and the correlation of the cross-model ensemble mean is shown in in filled black circles. The grey lines in each panel denote the $P > 0.1$ significance level (against a white noise with sample size $n = 158$, one-tailed test). A scatter plot similar to that in **a** for AMOC and T_{NA} versus AMOC and S_S is shown in Fig. 3b.

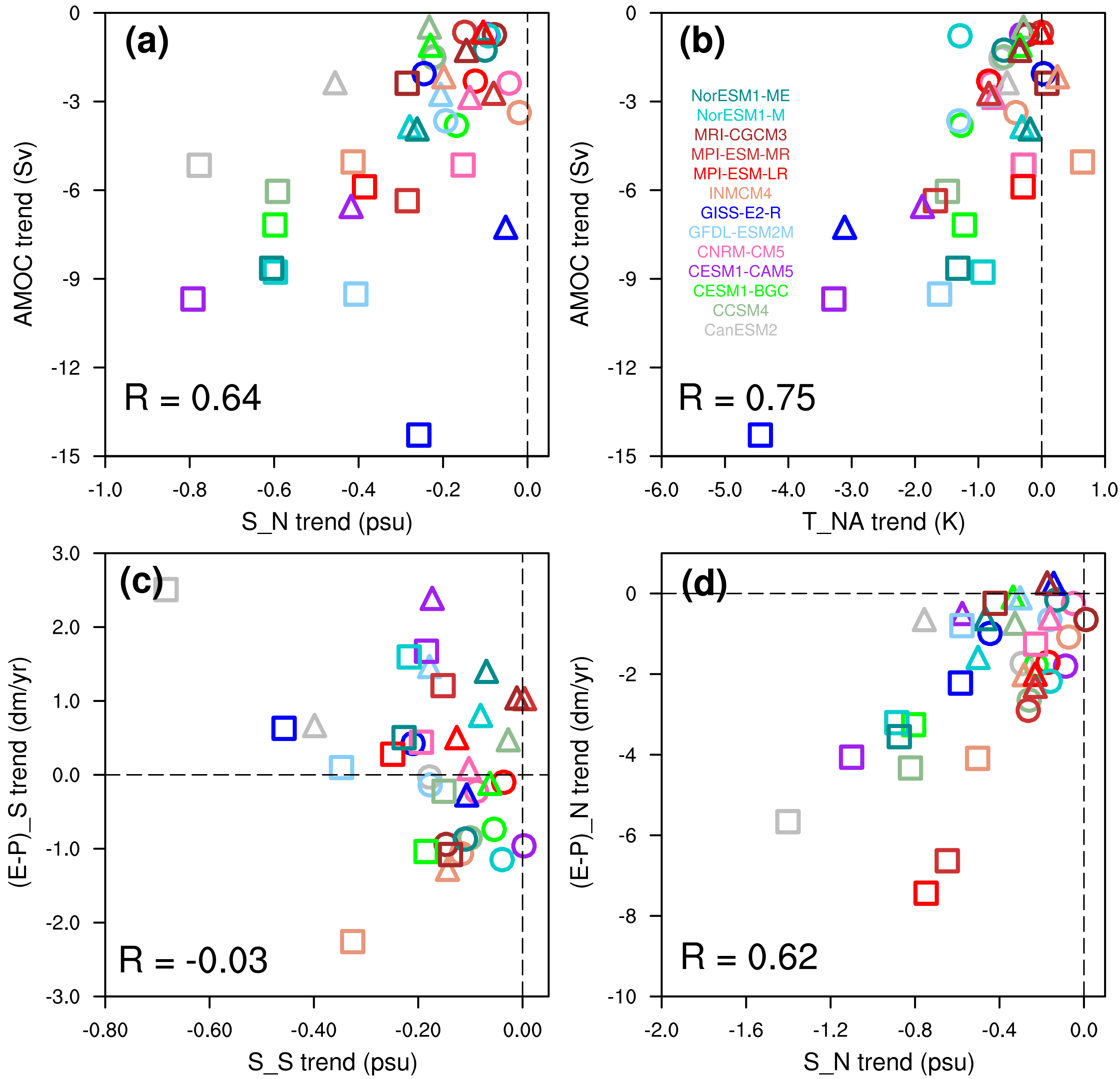

Extended Data Fig. 6 | Trends in AMOC, fingerprint indices and E−P. a–d, Cross-model scatter plots between the trends of the fingerprint indices and AMOC transport in the historical run (1861–2018, circles, with the period 2006–2018 using the RCP8.5 scenario) and for the future period 2019–2100 in RCP4.5 (triangle) and RCP8.5 (square) scenarios with the cross-ensemble correlations *R* shown in the lower left corners of the panels. **a**, AMOC versus S_N ($R=0.64$). **b**, AMOC versus T_{NA} ($R=0.75$). **c**, $(E-P)_S$ versus S_S ($R=-0.03$). **d**, $(E-P)_N$ versus S_N ($R=0.62$, for comparison with 'S' in **c**, here 'N' represents the difference of North Atlantic with North Pacific). Panel **c** shows no correlation between the trends of local $(E-P)_S$ and S_S, in contrast to the AMOC (Fig. 3c), suggesting the AMOC as the dominant driving force. By contrast, **d** shows that E−P is a strong forcing of salinity pile-up in North Atlantic, comparable with AMOC (**a**). The *R* value is calculated without the CanESM2 model (grey), which appears to be an outlier model for the trends of AMOC and all the indices, with the $P>0.1$ significance level as $R=0.22$ (against a white noise with sample size $n=36$, one-tailed test).

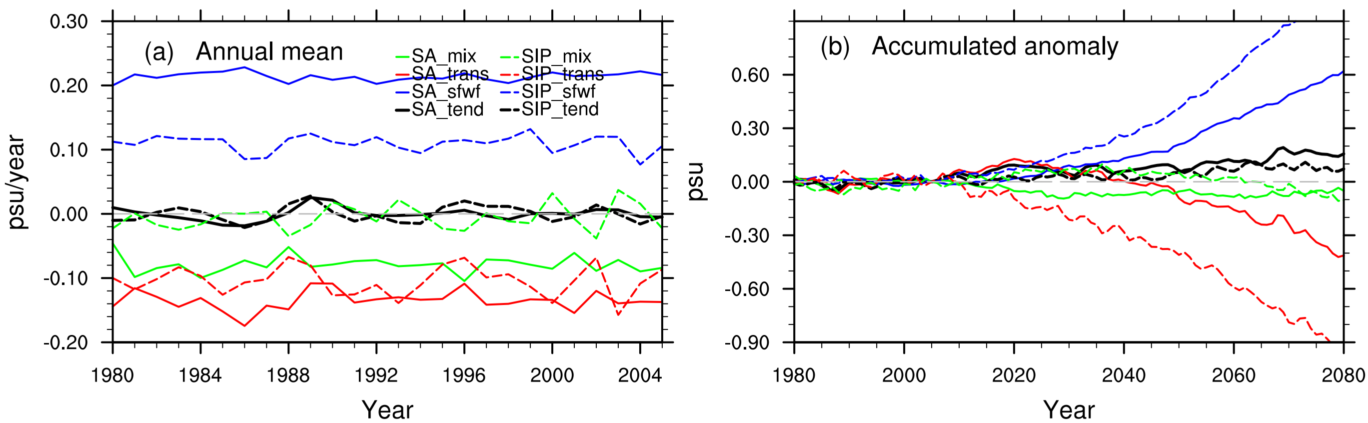

Extended Data Fig. 7 | Salinity budget in a coupled model. a,**b**, Subtropical (10° S–30° S) upper-ocean (0–200 m) basin mean salinity budget for an RCP8.5 simulation of CESM-LE. **a**, Historical period (1980–2005) annual mean salinity budget (psu year^{-1}). **b**, Accumulated anomaly (relative to the 1980–2005 mean, psu) for the comparison between the South Atlantic and Indo-Pacific. The four terms in the legend indicate the contributions of the tendency ('tend'), transport divergence ('trans'), surface E–P ('sfwf') and mixing ('mix'). The major feature is a smaller increase in salinity divergence (less-negative anomaly) in the South Atlantic than in the Indo-Pacific and North Atlantic. This smaller increase is caused by the weakened AMOC transport.

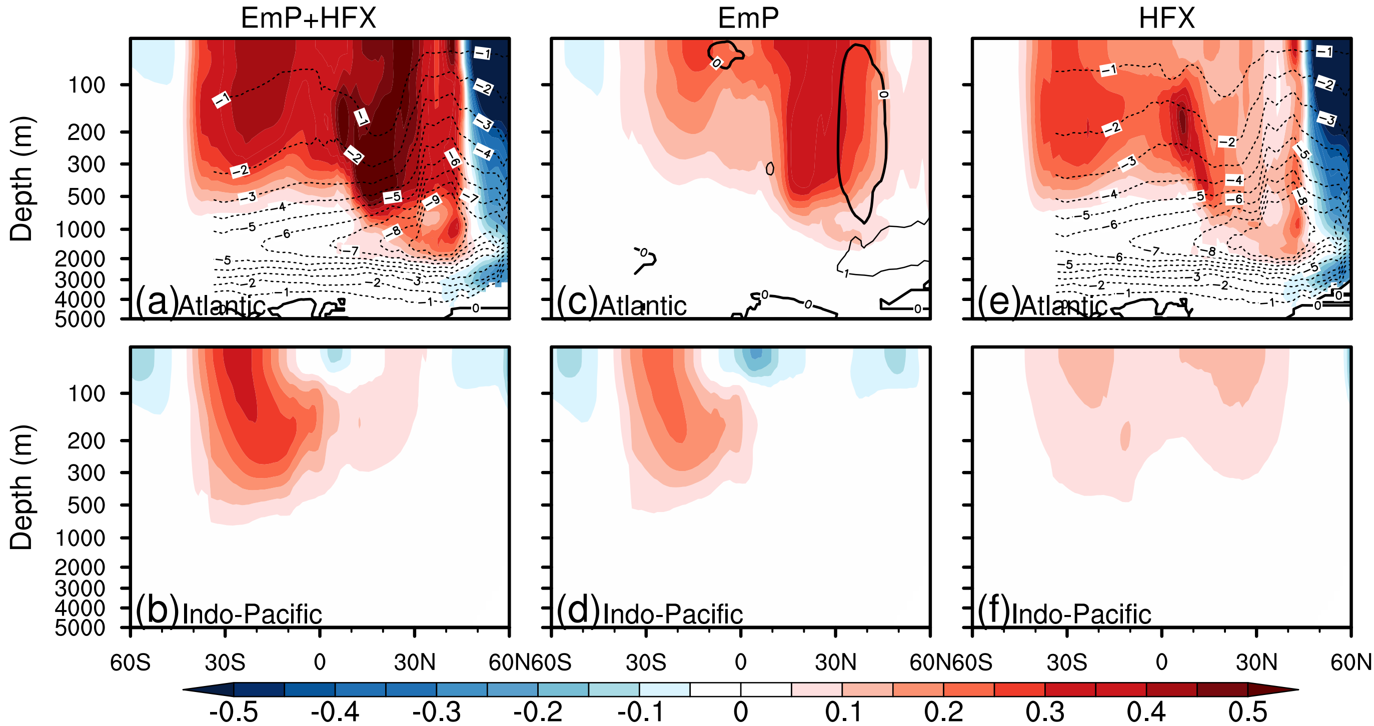

Extended Data Fig. 8 | Ocean salinity trend in the sensitivity experiments. a–f, Ocean zonal mean salinity trend (psu century^{-1}, colour scale) in the ocean model sensitivity simulations in the Atlantic (**a**,**c**,**e**) and Indo-Pacific (**b**,**d**,**f**) for experiments EmP+HFX (**a**,**b**), EmP (**c**,**d**) and HFX (**e**,**f**). The trends in the AMOC are also plotted (Sv century^{-1}, contours) in **a**, **c** and **e**.

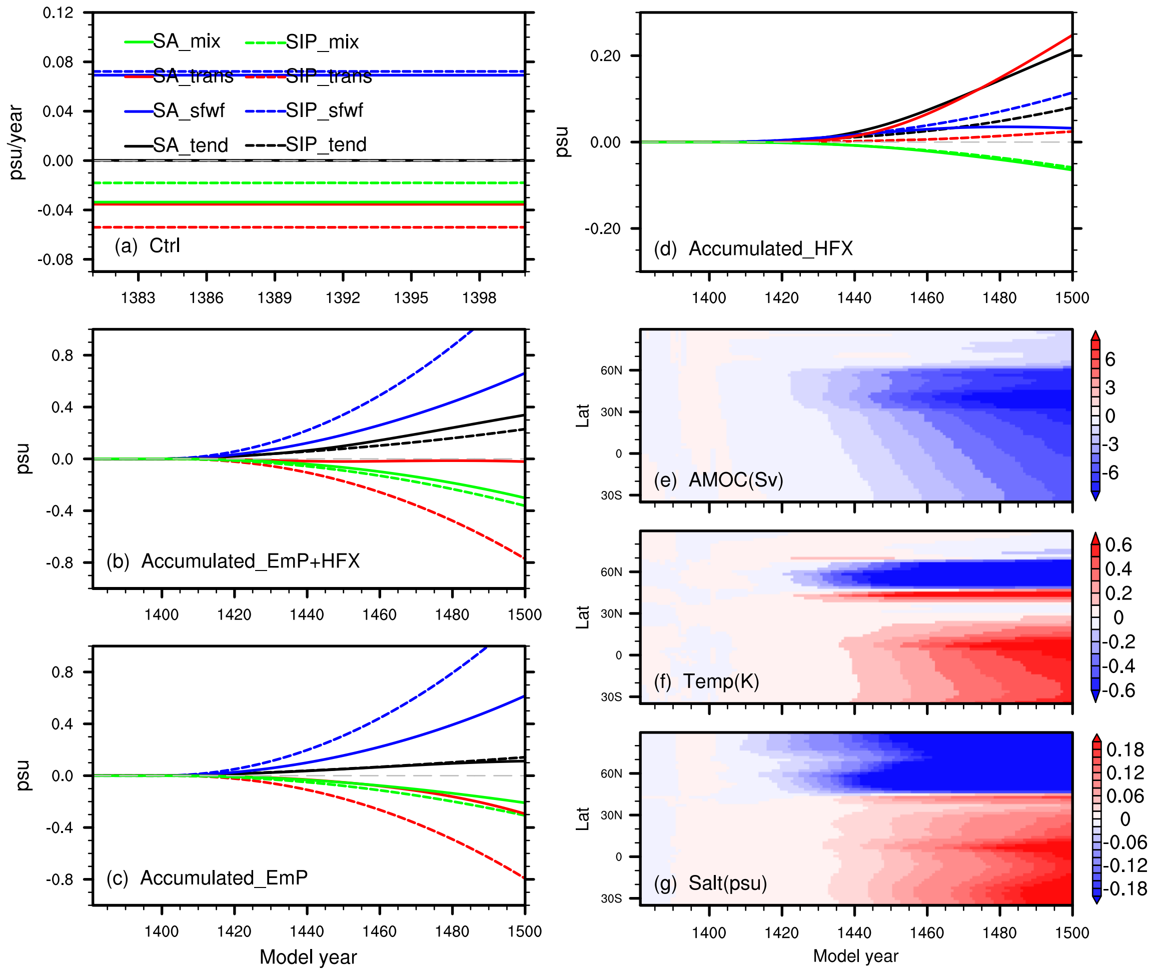

Extended Data Fig. 9 | Evolution in the sensitivity experiments. a–g, Upper ocean (0–300 m) basin mean salinity budget for the subtropics (10° S–34° S) for ocean-alone sensitivity experiments. **a**, Control run annual mean budget. **b**,**c**,**d**, The accumulated anomalies (relative to control) for South Atlantic and South Indo-Pacific in experiments EmP+HFX (**b**), EmP (**c**) and HFX (**d**). Note the different vertical scales for each experiment. Over the South Atlantic, in HFX, the salinity divergence is reduced (positive in Extended Data Fig. 9d) by the weakening AMOC. With the combined forcing in EmP+HFX, the divergence of salinity transport still increases slightly over the South Atlantic (slightly negative in Extended Data Fig. 9b) as in the coupled model (Extended Data Fig. 7b), because the E−P forcing increases the salinity gradient and, in turn, the mean advection on the salinity anomaly and finally, the salinity divergence (Extended Data Fig. 9c). **e**,**f**,**g**, The time–latitude evolution of the AMOC (**e**) and upper (0–300 m) South Atlantic temperature (**f**) and salinity (**g**) in HFX shows a coherent penetration southward. The salinity response appears to respond earlier in the South Atlantic, likely caused by the divergence of the oceanic transport and salinity gradient. Therefore, the AMOC slowdown in the South Atlantic reduces salinity transport divergence, leading to the salinity pile-up there.

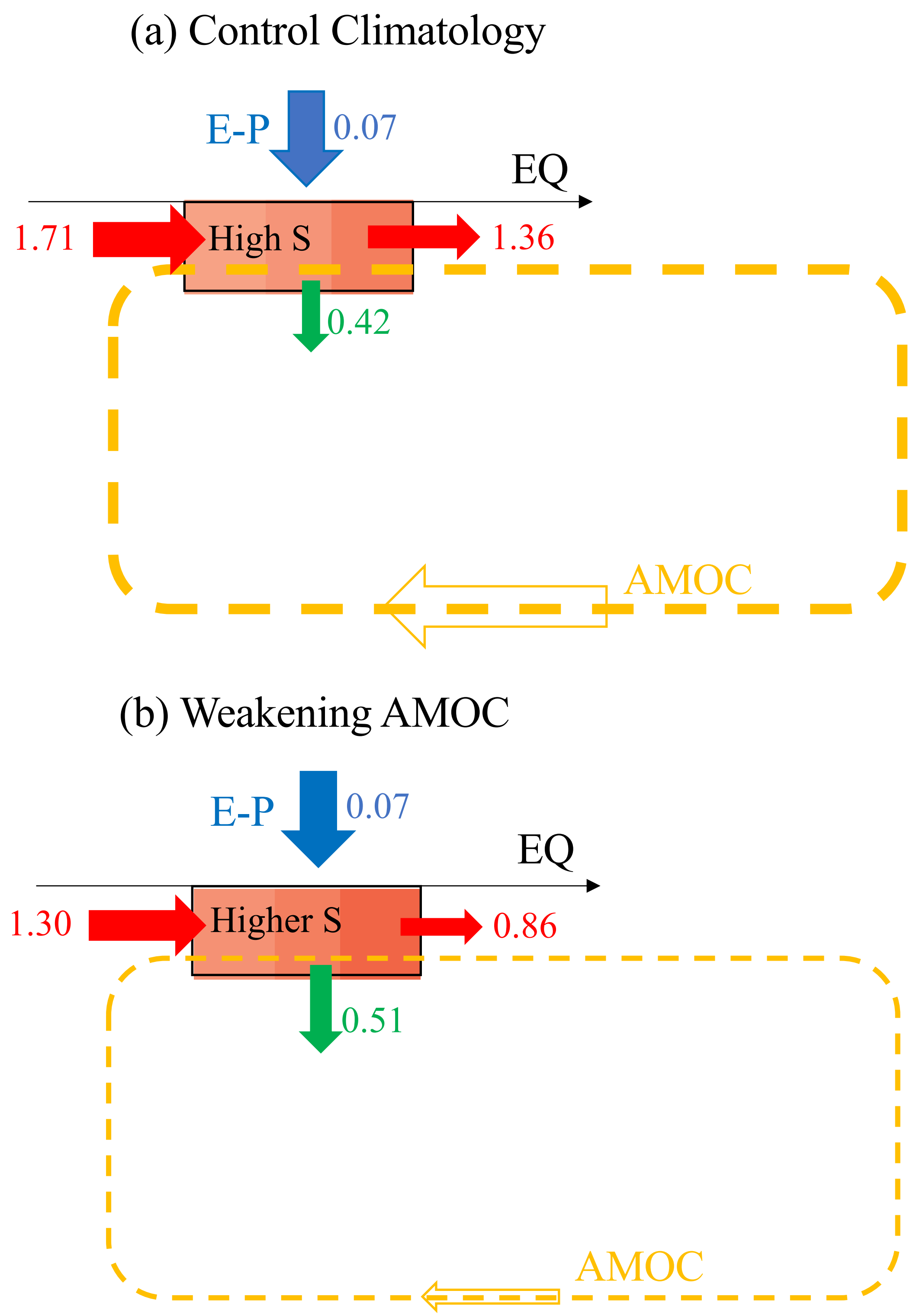

Extended Data Fig. 10 | Mechanism of South Atlantic salinity pile-up. a,**b**, Mechanism illustrated by the salinity budget of the upper South Atlantic in the ocean model experiment HFX (psu year^{-1}). Control climatology (**a**) and HFX experiment (**b**) with a weakening AMOC (climatology of the last 20 years). Blue arrows are net E−P flux, red arrows indicate meridional salinity transport and green arrows indicate vertical salinity transport (including a small contribution by mixing). Red shadings are the symbolic salinity gradient across the South Atlantic (note that the northern side is climatologically saltier than the southern side, also see Extended Data Fig. 2c). The accumulated salinity budget of HFX is shown in Extended Data Fig. 9d. The salinity pile-up is caused primarily by the reduced northward salinity transport associated with the reduced AMOC, which is more reduced downstream (northern side) than upstream (southern side) because of a greater mean salinity in the former. This AMOC-induced salinity pile-up is robust for the South Atlantic overall basin mean, while the detailed pattern of salinity changes can be affected by other processes, especially in the coupled model.